AIChE

Simulation of a Slurry-Bubble Column Reactor for Fischer-Tropsch Synthesis Using Single-Event Microkinetics

Gisela Lozano-Blanco and Joris W. Thybaut
Laboratory for Chemical Technology, Ghent University, Krijgslaan 281, S5 B-9000 Ghent, Belgium

Karine Surla and Pierre Galtier
Institut Français du Pétrole, B.P. 3, 69390 Vernaison, France

Guy B. Marin
Laboratory for Chemical Technology, Ghent University, Krijgslaan 281, S5 B-9000 Ghent, Belgium

DOI 10.1002/aic.11786
Published online June 29, 2009 in Wiley InterScience (www.interscience.wiley.com).

A single-event microkinetic model for Fischer-Tropsch synthesis including the water-gas shift reaction has been implemented in a one-dimensional, two-bubble class, heterogeneous model with axial effective diffusion to study the performance of a commercial slurry bubble column reactor. Mass balance equations are solved for every species in the reaction network in the large bubbles, small bubbles, and slurry phase, whereas the energy balance is applied to the slurry phase. The catalyst concentration profile is described by a sedimentation-dispersion model. The combination of microkinetics that generate net production rates for the individual reaction products and hydrodynamics allows describing detailed concentration profiles along the reactor axis as a function of operating conditions and design parameters. As example, the effects of catalyst loading, syngas feed flow rate, inlet temperature, or hydrogen to carbon monoxide inlet ratio on the individual hydrocarbons are investigated. To our knowledge, no reactor model in literature is able to describe detailed compositions at the level described by the reactor model developed in this work. © 2009 American Institute of Chemical Engineers *AIChE J*, 55: 2159–2170, 2009
Keywords: slurry bubble column reactor, Fischer-Tropsch synthesis, iron, single-event, microkinetic modeling

Introduction

Fischer-Tropsch synthesis is the catalytic hydrogenation of carbon monoxide to hydrocarbon fuels and chemicals. Increasing prices and depleting reserves of crude oil together with the necessity of monetizing ''stranded'' natural gas resources have resurged the interest in Fischer-Tropsch synthesis in the last decades.[1,2] Different reactor types are used for the commercial operation of Fischer-Tropsch synthesis. In particular, for the low temperature operation regime (473–530 K), one of the reactor types used commercially is the slurry bubble column reactor (SBCR) due to the excellent heat transfer characteristics and the lower operation costs when compared with other reactor types such as the multitubular-fixed bed reactor especially when iron is used as catalyst.[2,3] The Sasol Slurry Phase Distillate™ (Sasol SPD™)

Correspondence concerning this article should be addressed to J. W. Thybaut at Joris.Thybaut@UGent.be.

process was developed for an iron-based catalyst in Sasolburg. Currently, a more active cobalt-based catalyst is used in Qatar and will be used in Nigeria to convert natural gas into diesel, naphta, and liquefied petroleum gas in the same process.[2]

The most optimal flow operation regime is the churn-turbulent or heterogeneous regime induced at high gas throughputs, that is, superficial gas velocities above 0.1 m/s.[4] This regime is characterized by a bimodal bubble size distribution. Small bubbles coalesce in bubble clusters denoted as large bubbles, which rise through the column at a velocity in the range of 1–2 m/s. The small bubbles and catalyst particles are entrained by the liquid.[4–8]

The two-bubble class hydrodynamic model with axial effective diffusion investigated by Krishna and coworkers[4–8] and Dudukovic and coworkers[9,10] accounts for the different flow patterns of the two bubble classes, the liquid and the catalyst particles. This reactor model is applied also in this work to perform simulations of a commercial reactor with the same dimensions as the reactor used at Sasolburg with an iron-based catalyst.

Until now, none of the industrial SBCR models in the literature includes a fundamental kinetic model containing net production rates for the individual species in the model equations. Typically, simplified kinetic models and/or empirical product distribution models have been applied to calculate the product selectivities.[5,8–14] Recently, a Single-Event Microkinetic (SEMK) model was developed. This model was initially applied for an iron-based catalyst but can be extended to cobalt-based catalysts.[15,16] The single-event concept allows calculating rates of individual elementary steps with a limited number of kinetic parameters. Combining these microkinetics with the hydrodynamics of a real-life industrial reactor allows calculating detailed product distributions along the reactor as a function of the reactor design parameters and operating conditions.

Reactor Model

The SBCR is modeled according to the scheme displayed in Figure 1. Three phases are considered: large bubbles, small bubbles, and the liquid containing the catalyst particles in suspension also denoted as slurry phase. The gas phase enters the reactor at the bottom and is dispersed into the slurry phase by a distributor plate. Gas and slurry phase operate in continuous and cocurrent mode. The Fischer-Tropsch reaction is highly exothermic. The temperature inside the reactor is controlled by means of internal cooling tubes.

In the churn-turbulent flow regime, large bubbles with a diameter between 20 and 70 mm rapidly traverse the column and churn-up the slurry phase together with the small bubbles with a diameter between 1 and 10 mm. The slurry phase and the small bubbles are highly backmixed. The large bubbles flow can be described by a close to ideal plug-flow model, whereas the flow of the small bubbles and the slurry phase are more adequately described by an axial dispersion model.[3]

Model equations

Transient mass balance equations based on an axial dispersion model are applied for every species in the large bubbles, small bubbles, and slurry phase. The energy balance is applied to the slurry phase to calculate the reactor temperature. The catalyst axial concentration profile is calculated by a sedimentation-dispersion model.[17]

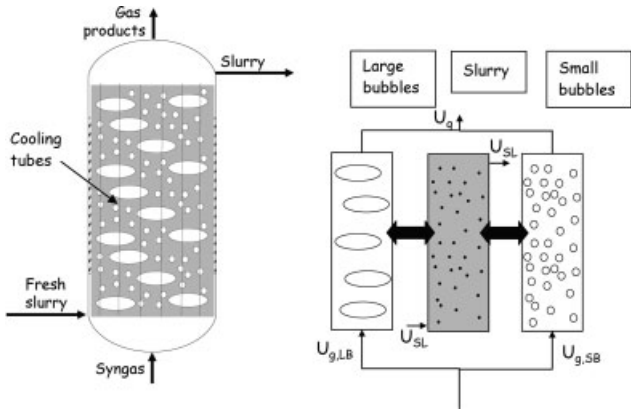

Figure 1. Schematic representation of a SBCR and the different phases assumed in the reactor model.

The main model assumptions applied in the reactor model equations are:

(1) gas–liquid mass transfer resistance is located in the liquid phase,

(2) gas phase and catalyst particles are in thermal equilibrium with the liquid phase,

(3) the catalyst particle diameter is small enough so that intraparticle temperature and concentration gradients are negligible,

(4) local values are applied for gas and liquid hold-ups, Peclet numbers and superficial gas velocity.

Hydrodynamic, transport parameters, and physical properties used in the simulations are discussed in the following sections.

Mass balances for the *ncomp* reactants and products in the large bubbles, small bubbles, and slurry phase, and energy balance for the slurry phase, are applied around a differential volume element of the reactor displayed in Figure 1. A mass balance for the catalyst particles is included by a sedimentation-dispersion model. This results in a set of 3 *ncomp* + 2 second-order partial differential equations. The balance equations account for the accumulation, dispersion, convection, and mass and energy transfer terms of the corresponding phases. The definition of the other dimensionless parameters appearing in the equations is given in the nomenclature section.

The mass balance for species j in the large bubbles is written as:

$$\varepsilon_{LB}\frac{\partial y_{LB,j}}{\partial \tau}=\frac{\varepsilon_{LB}}{Pe^{g}_{LB}}\frac{\partial}{\partial \xi}\left(\frac{\partial y_{LB,j}}{\partial \xi}\right)-\frac{u_{LB}}{u^{0}_{g}}\frac{\partial y_{LB,j}}{\partial \xi}-St^{g}_{LB,j}(y_{LB,j}-x_j) \tag{1}$$

where ε_{LB} is the hold-up of the large bubbles, $y_{LB,j}$ is the dimensionless concentration of species j in the large bubbles,

u_{LB} the superficial gas velocity of the large bubbles, u_g^0 the initial total superficial gas velocity, $St^g_{LB,j}$ the gas–liquid Stanton number for species j in the large bubbles, x_j is the dimensionless concentration of species j in the liquid phase, τ is the dimensionless time, and ξ the dimensionless axial coordinate.

The mass balance for species j in the small bubbles is analogous to that in the large bubbles:

$$\varepsilon_{SB}\frac{\partial y_{SB,j}}{\partial \tau}=\frac{\varepsilon_{SB}}{Pe^g_{SB}}\frac{\partial}{\partial \xi}\left(\frac{\partial y_{SB,j}}{\partial \xi}\right)-\frac{u_{SB}}{u_g^0}\frac{\partial y_{SB,j}}{\partial \xi}-St^g_{SB,j}(y_{SB,j}-x_j) \tag{2}$$

The mass balance for species j in the slurry phase includes a reaction term in addition to the diffusion, convection, and phase transfer terms:

$$\varepsilon_{SL}\frac{\partial x_j}{\partial \tau}=\frac{\varepsilon_{SL}}{Pe_L}\frac{\partial}{\partial \xi}\left(\frac{\partial x_j}{\partial \xi}\right)-\frac{u_{SL}}{u_g^0}\frac{\partial x_j}{\partial \xi}+$$
$$St^L_{SB,j}(y_{SB,j}-x_j)+St^L_{LB,j}(y_{LB,j}-x_j)-\varepsilon_{cat}\sum_{i=1}^{nr}\upsilon_{ij}\hat{r}_i(x_j,\theta_k,\Theta\ldots) \tag{3}$$

where ε_{cat} is the local catalyst hold-up in the slurry, υ_{ij} is the stoichiometric coefficient for species j in the i-th reaction, $\hat{r}_i$ the dimensionless reaction rate for the i-th reaction, θ_k is the dimensionless surface concentration of species k, and Θ the dimensionless temperature.

The energy balance in the slurry phase is:

$$\varepsilon_{SL}\frac{\partial \Theta}{\partial \tau}=\frac{\varepsilon_{SL}}{Pe_H}\frac{\partial}{\partial \xi}\left(\frac{\partial \Theta}{\partial \xi}\right)-\frac{u_{SL}}{u_g^0}\frac{\partial \Theta}{\partial \xi}-St_H(\Theta-1)$$
$$+\varepsilon_{cat}\sum_{i=1}^{nr}Be_i\hat{r}_i(x_j,\theta_k,\Theta\ldots) \tag{4}$$

Be_i being the dimensionless heat of reaction for the i-th reaction.

The sedimentation-dispersion model[17] is applied to the catalyst particles in the slurry phase:

$$\frac{\partial \varepsilon_{cat}}{\partial \tau}=\frac{1}{Pe_{cat}}\frac{\partial}{\partial \xi}\left(\frac{\partial \varepsilon_{cat}}{\partial \xi}\right)+\left(\frac{u_{CT}}{u_g^0}-\frac{u_{SL}}{u_g^0(1-\varepsilon_g)}\right)\frac{\partial \varepsilon_{cat}}{\partial \xi} \tag{5}$$

where u_{CT} is the settling velocity of the catalyst,[17] defined in the following section.

The initial and boundary conditions for Eqs. 1–5 are given in Table 1. Boundary conditions of the Danckwerts type[18] are applied. Before the reactor start-up, that is, at $\tau < 0$, the catalyst is loaded in the reactor and an inert gas flows continuously through a paraffin wax establishing an initial catalyst axial distribution $\varepsilon^0_{cat}(\xi)$. After the reactor start-up, it is assumed that catalyst particles are neither added nor removed from the reactor. Synthesis gas is allowed at $\tau \geq 0$. Large and small bubbles at the reactor inlet contain only reactants and the liquid is assumed to be saturated with the gas phase. According to Mills et al.,[12] the remaining boundary condition for the sedimentation-dispersion model is the overall catalyst balance written as:

Table 1. Initial and Boundary Conditions for the SBCR Model Equations (Eqs. 1–5)

Initial Condition ($\tau = 0$)	Reactor Inlet ($\xi = 0$)	Reactor Outlet ($\xi = 1$)
$y_{LB,j}=y^0_{g,j}$	$\frac{\varepsilon_{LB}}{Pe^g_{LB}}\frac{dy_{LB,j}}{d\xi}=\frac{u_{LB}}{u_g^0}y_{LB,j}-\frac{u^0_{LB}}{u^0_g}y^0_{LB,j}$	$\frac{dy_{LB,j}}{d\xi}=0$
$y_{SB,j}=y^0_{g,j}$	$\frac{\varepsilon_{SB}}{Pe^g_{SB}}\frac{dy_{SB,j}}{d\xi}=\frac{u_{SB}}{u_g^0}y_{SB,j}-\frac{u^0_{SB}}{u^0_g}y^0_{SB,j}$	$\frac{dy_{SB,j}}{d\xi}=0$
$x_{L,j}=y^0_{g,j}$	$\frac{\varepsilon_{SL}}{Pe_L}\frac{dx_{L,j}}{d\xi}=\frac{u_{SL}}{u_g^0}x_{L,j}-\frac{u^0_{SL}}{u^0_g}x^0_{L,j}$	$\frac{dx_{L,j}}{d\xi}=0$
$\varepsilon_{cat}(\xi)=\varepsilon^0_{cat}(\xi)$	$\frac{d\varepsilon_{cat}}{d\xi}+Bo_{cat}\varepsilon_{cat}=0$	
$\Theta=T^0/T_w$	$\frac{\varepsilon_{SL}}{Pe_L}\frac{d\Theta}{d\xi}=\frac{u_{SL}}{u_g^0}\Theta-\frac{u^0_{SL}}{u^0_g}\Theta^0$	$\frac{d\Theta}{d\xi}=0$

$$\bar{\varepsilon}_{cat}=\int_0^1\varepsilon_{cat}(\xi)d\xi \tag{6}$$

where $\bar{\varepsilon}_{cat}$ is the known average catalyst hold-up in the reactor.

Physical properties and hydrodynamic parameters

The physical properties of the slurry phase are calculated with the expressions proposed by Deckwer et al.[19,20] The properties of the pure liquid, gas and catalyst adopted by de Swart and Krishna[5] are also applied in this work. In particular, eicosane, an *n*-alkane with 20 carbon atoms, was used to calculate the physical properties of the liquid phase. The density of the iron catalyst is taken equal to 1957 kg/m^3 as reported by Lox et al.[21] The adopted catalyst diameter is 50 μm as it is normally used in SBCR, in order to guarantee the absence of intraparticle temperature and concentration gradients.[5,22]

Standard reaction enthalpies are calculated from the standard enthalpies of formation of reactants and products at the operating temperature. Benson's group additivity method[23] is applied in an in-house code to calculate thermodynamic properties of alkanes and alkenes, and tabulated values[24] are used for the nonhydrocarbon molecules. In this code, groups are identified from a numerical representation of the alkanes and alkenes.[15,16]

The diffusivities of the different species (solutes) in the liquid L (solvent) required for calculating the mass transfer coefficients were obtained as[25]:

$$D_{L,solute}=\frac{7.410^{-8}M^{0.5}_{w,L}T}{\eta_L v^{0.6}_{solute}} \tag{7}$$

where $M_{W,L}$ is the molecular mass of the liquid, T the temperature, η_L the viscosity of the solvent, and v_{solute} the molar volume of the solute at normal boiling point estimated using the Le Bas additive volume method.[26]

Henry coefficients for all the components were calculated as:

$$He_i=He_i^{\infty}\exp\left[\bar{v}_i^{\infty}(p-p_{j,sat})/RT\right] \tag{8}$$

where He_i^{∞} is the Henry coefficient at infinite dilution, $\bar{v}_i^{\infty}$ is the partial molar volume at infinite dilution, $p_{j,sat}$ is the vapor

pressure of saturated pure j (solvent) at the temperature T, and R is the universal gas constant. The exponential factor is known as the Poynting factor, Φ_i, and represents the pressure effect correction to the liquid phase fugacity.[27]

Henry coefficients and partial molar volumes at infinite dilution in eicosane for hydrogen, carbon monoxide, water, carbon dioxide, alkanes, and alkenes involved in the reaction network, and vapor pressures and liquid molar volumes for the alkanes and alkenes were calculated using asymptotic behavior correlations developed by Marano and Holder.[28]

Vapor phase fugacity coefficients close to unity were calculated with the Peng-Robinson equation of state[26,28] at industrial operating conditions for hydrocarbons up to 20 carbon atoms. Hence, for the gas phase, ideal behavior was assumed.

The molar flow rate in the gas phase changes due to the reaction. Rigorously, the superficial gas velocity is obtained from the mass balance considering all the species consumed and generated in the gas phase. However, this introduces complexities in the numerical solution and the simplification proposed by Deckwer et al.[20] based on the expansion factor as defined by Levenspiel[29] and usually applied in literature[5,8,13] has been adopted, that is:

$$u_g = u_g^0(1 + \alpha_c X_{CO+H_2}) \tag{9}$$

Typical contraction factors, α_c, lie between -0.5 and -0.65.[20] A contraction factor equal to -0.5 has been used in the simulations shown in this work.

One of the most important hydrodynamic parameters is the gas hold-up of the large and small bubbles. In the churn-turbulent regime, the gas hold-up and superficial gas velocity of the small bubbles are assumed to be equal to their values at the transition point from the homogeneous to the heterogeneous regime, ε_{trans} and $u_{g,trans}$, respectively.[30] For the slurry phase, a constant superficial velocity is assumed along the reactor.

The hydrodynamic, mass, and heat transfer parameters used in the reactor model are given in Table 2. Large bubbles flow can be described by a close to ideal plug-flow model. For this purpose, a Peclet number, Pe_{LB}, equal to 100 has been adopted.[5] The small bubbles are entrained in the liquid and follow the same mixing behavior as the slurry phase and, hence, the axial effective diffusion for the small bubbles E_{SB} is assumed equal to that of the liquid E_L[5] defined in Table 2.

Single-Event Microkinetics (SEMKs)

The SEMK model developed in a previous work[15,16] for a commercial, precipitated iron catalyst is incorporated in the reactor model. The SEMK methodology allows reducing the number of parameters by applying the reaction family concept.[36] The rate of every elementary step is explicitly accounted for and consequently net production rates for every species in the reaction network are included in the reactor model Eqs. 3 and 4. The reactor network considered in elementary steps is given in Table 3. The "carbene" mechanism[37] was adopted for the chain growth occurring on the carbide phase of the catalyst, which is the active phase for iron-based Fischer-Tropsch synthesis, and the "formate" mechanism[38] for the water-gas shift occurring on the iron oxide phase of the catalyst.

Single-event kinetic parameters were estimated by model regression to experimental data obtained in a tubular fixed-bed reactor at steady-state under isothermal and nondeactivating conditions.[39] The range of operating conditions studied varied from 523 to 623 K, 0.6 to 2.1 MPa, and 2 to 6 mol/mol H_2 to CO inlet ratio. The intrinsic character of the observed reaction kinetics was verified by applying the criteria of Weisz and Prater and Mears.[40]

The net formation rate of a particular species is obtained by summation of the rates of the elementary steps in which these species are involved. For example, net formation rates for an alkane l and an alkene k with n carbon atoms are obtained from:

$$R_{alkane,l} = \sum_{i=1}^{nmalkyls} \frac{z}{2}\frac{\sigma_{gl,r}}{\sigma_{gl,\neq}} \tilde{k}_{re,M-alkyls} C_{M_{tot}} \theta_{M-C_nH_{2n+1},i\rightarrow l} \theta_{M-H} - \frac{z}{2}\frac{\sigma_{gl,r}}{\sigma_{gl,\neq}} \tilde{k}_{oa,alkanes} C_{M_{tot}} p_{C_nH_{2n+2,l}} \theta_M^2 \tag{10}$$

$$R_{alkene,k} = \frac{\sigma_{gl,r}}{\sigma_{gl,\neq}} \tilde{k}_{des,M-alkenes} C_{M_{tot}} \theta_{M-C_nH_{2n},j\rightarrow k} - \frac{\sigma_{gl,r}}{\sigma_{gl,\neq}} \tilde{k}_{chem} C_{M_{tot}} p_{C_nH_{2n},k} \theta_M \tag{11}$$

Within a reaction family, only symmetry effects can lead to differences in rate coefficients. These differences are captured by the ratio between the global symmetry number of the reactant $\sigma_{gl,r}$ and transition state $\sigma_{gl,\neq}$, corresponding to the number of the so-called single-events.[36] In the equations above, $\tilde{k}$ is the "single-event" rate coefficient which is unique for a given reaction family, $C_{M_{tot}}$ is the concentration of iron atoms in the carbide phase, and z is the number of nearest neighbor atoms surrounding a particular atom[41] of the catalyst, assumed equal to four.

Mass balances for the nint surface intermediates are also required:

$$\frac{d\theta_i}{d\tau} = R_i \tag{12}$$

The concentration of free iron in the carbide phase, and iron and oxygen atoms in the oxide phase of the catalyst, is calculated with the balance of atoms in both catalyst phases, as explained elsewhere.[15,16]

Numerical solution strategy

As mentioned previously, the reactor model is defined by 3 *ncomp* + 2 second order partial differential equations, that is, Eqs. 1–5, together with the boundary conditions given in Table 1 and Eq. 6, and nint ordinary differential equations with respect to time corresponding to the net formation rates of the surface intermediates, Eq. 12.

The ultimate objective is to describe the performance of the SBCR at steady-state operation. However, the model equations in transient form can be more easily solved. The steady-state model Eqs. 1–5 are second order ordinary differential equations subject to the boundary conditions given in Table 1, whereas the steady-state mass balance for the intermediates concentrations, Eq. 12, results in a set of nonlinear

Table 2. Hydrodynamic, Mass, and Heat Transfer Parameters Involved in the SBCR Model Equations (Eqs. 1–5 and Table 1)

Property[(source)]	Correlation
Gas hold-up at transition,[5] ε_{trans} (m^3_g/m^3_R)	$2.16\ \exp(-13.1\ \rho_g^{-0.1}\eta_L^{0.16}\sigma^{0.11})\ \exp(-5.86\varepsilon_{cat})$
Superficial gas velocity at transition,[5] $u_{g,trans}$ (m/s)	$V_{SB}\varepsilon_{trans}$
Rise velocity of small bubbles,[31] V_{SB} (m/s)	$2.25(\sigma/\eta_L)(\sigma^3\rho_L/g\eta_L^4)^{-0.273}\ (\rho_L/\rho_g)^{0.03}$
Large bubbles hold-up,[30,32] ε_{LB} (m^3_{LB}/m^3_R)*	$0.268u_{LB}^{0.58}/d_R^{0.18}\ (\rho_g/\rho_{g,ref})^{0.5}$
Slurry hold-up, ε_{SL} (m^3_{SL}/m^3_R)	$1-(\varepsilon_{LB}+\varepsilon_{SB})$
Mass transfer coefficient for species j for the small bubbles,[33] $k_{L,SB,j}$ (m/s)	$0.31\left(\frac{(\rho_g-\rho_{SL})\eta_{SL}g}{\rho_{SL}^2}\right)^{1/3}\left(\frac{\eta_{SL}}{\rho_{SL}D_{L,j}}\right)^{-2/3}$
Gas–liquid interfacial surface area for small bubbles,[31] a_{SB} (m^2/m^3)	$6\varepsilon_{SB}/d_{SB}$
Diameter of small bubbles,[34] d_{SB} (m)	$3g^{-0.44}\sigma^{0.34}\eta_L^{0.22}\rho_L^{-0.45}\rho_g^{-0.11}u_g^{-0.02}$
Volumetric mass transfer coefficient for species j for the large bubbles,[35] $(k_La)_{LB,j}$ (s^{-1})†	$0.5\varepsilon_{LB}\left(\frac{D_{L,j}}{D_{L,ref}}\right)^{0.5}$
Heat transfer coefficient,[20] α_{eff} ($w/m^2/K$)‡	$0.1(\rho_{SL}C_{p,SL}u_g)\left(\frac{u_g^3\rho_{SL}}{g\eta_{SL}}\right)^{-0.25}\left(\frac{\eta_{SL}c_{p,SL}}{\lambda_{SL}}\right)^{-0.5}$
Effective axial diffusion coefficient of the liquid phase,[20] E_L (m^2/s)	$0.768u_g^{0.32}d_R^{1.34}$
Effective axial diffusion coefficient of the catalyst,[17] E_{cat} (m^2/s)	$u_gd_R\frac{(1+8Fr^{0.55})}{13Fr}$
Settling velocity of the catalyst,[17] u_{CT} (m/s)	$u_{CT}=1.2u_{TS}\left(\frac{u_g}{u_{TS}}\right)^{0.25}\left(\frac{1-\varepsilon_{cat}}{1-\varepsilon^*_{cat}}\right)^{5/2}$
Terminal settling velocity of the catalyst,[17,20] u_{TS} (m/s)	$u_{TS}=\frac{Re\eta_L}{\rho_Ld_{cat}}$ $Re=\begin{cases} Ar/18 & \text{if}\quad Re\le 0.5 \\ (Ar/13.9)^{0.7} & \text{if}\quad Re>0.5 \end{cases}$
Mass fraction of catalyst,[5] W_{cat} (kg_{cat}/kg_{SL})	$W_{cat}=\frac{\rho_{cat}\varepsilon_{cat}}{\rho_L+\varepsilon_{cat}(\rho_{cat}-\rho_L)}$
Catalyst hold-up in the slurry,[20] ε^*_{cat} (m^3_{cat}/m^3_{SL})‖	$\varepsilon^*_{cat}=\frac{\rho_LW_{cat}}{\rho_{cat}-W_{cat}(\rho_{cat}-\rho_L)}$

*$\rho_{G,ref}=1.3$ kg/m^3. For columns with diameters d_R larger than 1 m, d_R must be set to 1 m.
†$D_{L,ref}=2\times10^{-9}$ m^2/s.
‡If u_g higher than 0.1 m/s, u_g must be set to 0.1 m/s.
‖For $\rho_{cat}=100$ kg/m^3.

algebraic equations. The bottleneck to solve the steady-state model is the nonlinearity of the algebraic equations coupled with the second order ordinary differential equations subject to the boundary conditions.

The transient equations have been successfully solved by applying the method of lines.[42] The partial differential equations are discretized in n node points by applying finite differences, Δh, for the spatial derivatives to obtain a set of ordinary differential equations with time as independent variable. As a result, reactor model equations are reduced to a set of ordinary differential equations and the boundary conditions to explicit algebraic equations.

The first and second spatial derivatives in the reactor model equations are written using central finite differences. The first derivatives in the boundary equations and in the net production rates of surface species are written using forward and backward finite differences for the first and last node, respectively.

The time variation for the concentration of the nint intermediate surface species occurs on a much shorter scale than the time variation for the concentration of the species in the gas and liquid phases. To decrease the stiffness of the equations and find a faster numerical solution, the pseudo-steady state approximation was applied to the surface species, that is, the concentration of the surface species is adapted to that of the observable species.

As a result, the reactor model is defined by 3 *ncomp* + 2 ordinary differential equations and *nint* nonlinear algebraic equations multiplied by the number of discretization points. These equations are solved with the numerical subroutine DASPK from Netlib library.[43]

To obtain adequate initial guesses for the concentration of the surface species, concentrations of carbon monoxide and hydrogen in the liquid phase are required. Hence, a first run is performed neglecting the reaction term in the model equations until species reach vapor–liquid equilibrium. Once the reactants are present in the liquid phase at every node point, the concentration of the surface species are calculated with the numerical routine DNSQE for solving nonlinear algebraic equations,[44] that is Eq. 12, from Netlib,[43] and are used as initial guesses in the subroutine DASPK. The use of concentration values for the reactants in the liquid phase along the reactor as initial condition was verified using a simple kinetic model, with and without considering reactants in the liquid phase, leading to the same solution in the steady-state.

After the initial convergence in the solver DASPK is achieved, the equations are integrated until steady-state

Table 3. Elementary Reaction Network* of Fischer-Tropsch Synthesis and Water-Gas Shift[16]

Elementary Reaction	
$H_2 + 2M \leftrightarrows 2MH$	(13)
$CO + 2M \leftrightarrows MMCO$	(14)
$MMCO + 3M \leftrightarrows MMMC + MMO$	(15)
$MMMC + MH \leftrightarrows MMMCH + M$	(16)
$MMMCH + MH \leftrightarrows MMCH_2 + 2M$	(17)
$MMCH_2 + MH \leftrightarrows MCH_3 + 2M$	(18)
$MMO + MH \leftrightarrows MOH + 2M$	(19)
$MOH + MH \leftrightarrows H_2O + 2M$	(20)
$MC_nH_{2n+1} + MMCH_2 \leftrightarrows MC_{n+1}H_{2n+3} + 2M$	(21)
$MC_nH_{2n+1} + MH \leftrightarrows C_nH_{2n+2} + 2M$	(22)
$MC_nH_{2n+1} + M \leftrightarrows MC_nH_{2n} + MH \ (n \geq 2)$	(23)
$MC_nH_{2n} \rightleftarrows C_nH_{2n} + M \ (n \geq 2)$	(24)
$H_2O + \underline{M} + \underline{O} \leftrightarrows \underline{M}—OH + \underline{O}—H$	(25)
$CO + \underline{M} \leftrightarrows \underline{M}—CO$	(26)
$\underline{M}—CO + \underline{O}—H \leftrightarrows \underline{O}—CHO—\underline{M}$	(27)
$\underline{O}—CHO—\underline{M} + \underline{M}—OH + \underline{O} \leftrightarrows \underline{O}—COOH—\underline{M} + \underline{O}—H + \underline{M}$	(28)
$\underline{O}—COOH—\underline{M} \leftrightarrows CO_2 + \underline{O}—H + \underline{M}$	(29)
$2\underline{O}—H \leftrightarrows H_2 + 2\underline{O}$	(30)

*The underlined atoms denote atoms belonging to the metal oxide lattice.

conditions. Only steady-state results are reported in the following section.

The physical properties and the thermodynamics of all the components are assumed constant during the calculation. This together with the Stanton numbers and the parameters for the catalyst sedimentation-dispersion model are calculated with the average superficial gas velocity and temperature along the reactor. This simplification improves the solver efficiency. The program runs iteratively until the average temperature and superficial gas velocity values match the values used in the previous iteration. Typically, two or three iterations are required to obtain convergence with respect to the average values.

Considering 45 node points for the discretization of the second order spatial derivatives and performing the simulations for a reaction network containing hydrocarbons with a maximum carbon number of 10, the total number of equations to be solved amounts to 4300 corresponding to 52 species: 23 gas and liquid phase components and 29 surface species. On a Pentium IV, CPU 2.4GHz and 512MB RAM, a typical simulation takes about 3 h time.

Simulation Results and Discussion

Simulations have been performed for an industrial reactor with the same size as the SBCR used at Sasolburg[2] for a reaction network containing *n*-alkanes and 1-alkenes with a maximum carbon number of 10. Because of the carbon number limitation set on the reaction network, tail artifacts are observed for the species with the last carbon number, that is, 10 in this case. Species with 10 carbon numbers express in reality species with carbon number 10 onwards. Hence, in the product distribution plots, only species up to carbon number 9 are shown. Using 45 node points in a uniform mesh size, the length of each section Δh corresponds to 0.5 m. The input parameters used in the simulations are given in Table 4.

The validation of the simulation results is limited to their comparison with generally reported trends[5,10–14,45] due to the lack of more specific data. The acquisition of such data goes beyond the scope of the current work.

Once the gas is injected at the bottom of the SBCR, large bubbles and small bubbles form and follow independent velocity and flow patterns, as explained in a previous section. Gas hold-up is a relevant hydrodynamic parameter which behavior as a function of the concentration of catalyst particles or column diameter (*vide* equations in Table 2) has been extensively studied.[8,30,31,45] For the operating conditions given in Figure 2, gas hold-up for large and small bubbles is 0.15 m^3/m^3 and 0.06 m^3/m^3, respectively, at the bottom of the reactor. For the large bubbles, the gas hold-up decreases along the column reaching the value of 0.13 m^3/m^3 at the reactor outlet due to the gas volume contraction of the Fischer-Tropsch reaction.

Including microkinetics in the reactor simulations provides detailed concentration profiles along the reactor axis at steady-state operation. In Figure 2, the axial dimensionless concentration profiles of carbon monoxide, hydrogen, carbon

Table 4. Reactor Geometry and Process Conditions

Geometry	
Reactor diameter, d_R (m)	5
Reactor height, H (m)	22
Volumetric heat exchange surface area of the cooling tubes, a_w (m^2_w/m^3_R)	13
Catalyst diameter, d_{cat} (m)	50×10^{-6}
Operating conditions in the column	
Pressure, p (bar)	30
Temperature in cooling tubes, T_w (K)	10 K below inlet temperature
Average catalyst hold-up in slurry, $\bar{\varepsilon}_{cat}$ (m^3_{cat}/m^3_{SL})	0.15, 0.25, 0.35
Properties of the inlet stream	
Syngas flow rate, F^0_{syngas} (m^3/s)*	2, 5, 8
Slurry flow rate, F^0_{SL} (m^3/s)	0.20
Pressure, p^0 (bar)	30
Temperature, T^0 (K)	523, 553, 583
Hydrogen to carbon monoxide ratio, $H_2/CO|^0$ (mol/mol)	0.5, 1, 2, 3

*Calculated at inlet conditions.

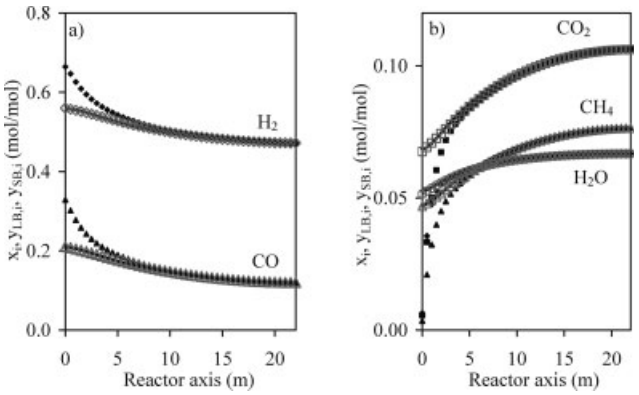

Figure 2. Dimensionless concentration vs. axial reactor coordinate for (a) carbon monoxide (▲) and hydrogen (◆) and (b) carbon dioxide (■), water (◆), and methane (▲), in the large bubbles, $y_{LB,i}$, (closed large symbols), small bubbles, $y_{SB,i}$, (gray open symbols), and liquid phase, x_i, (closed small symbols), calculated with Eqs. 1–6 and Table 1 at the inlet and design conditions given in Table 4 with T^0 = 553 K, $\bar{\varepsilon}_{cat}$ = 0.25, F^0_{syngas} = 5 m^3/s, and $H_2/CO|^0$ = 2.

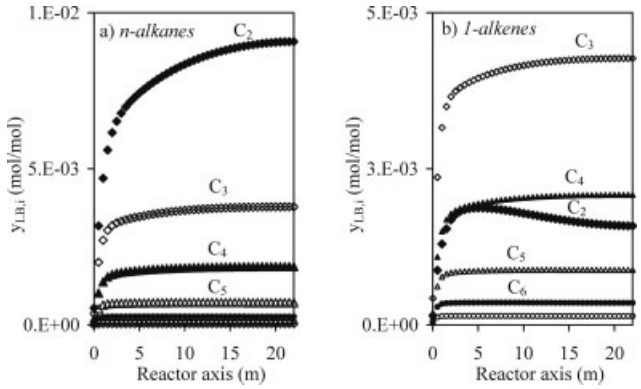

Figure 3. Dimensionless concentration profiles along the reactor axis for (a) *n*-alkanes and (b) 1-alkenes from carbon number 2 to 7 in the large bubbles calculated with Eqs. 1–6 and Table 1 at the inlet and design conditions given in Table 4 with T^0 = 553 K, $\bar{\varepsilon}_{cat}$ = 0.25, F^0_{syngas} = 5 m^3/s, and $H_2/CO|^0$ = 2.

Symbols: C_2 (◆), C_3 (◇), C_4 (▲), C_5 (△), C_6 (●), C_7 (○).

dioxide, water, and methane in the large bubbles, small bubbles, and slurry phase are displayed.

The small bubbles are always in equilibrium with the slurry phase at the design parameters used in this work. Mass transport phenomena control the reaction at the bottom of the reactor for the large bubbles and slurry phase in the sense that the concentrations in the slurry phase are not immediately in equilibrium with those in the large bubbles. This is related to the rate of mass transport with respect to the reactor hydrodynamics rather than with respect to the intrinsic chemical reaction rate. As observed in Figure 2, the concentrations between the species in the large bubbles and in the slurry phase are largely different. After a few meters, however, the species concentrations in the large bubbles reach equilibrium with those in the slurry phase, that is, the process becomes reaction controlled.

The axial dimensionless concentration profiles of *n*-alkanes and 1-alkenes up to carbon number 7 are shown in Figure 3 for the large bubbles only. The latter is the phase presenting higher concentrations in absolute terms as discussed below. The concentration profiles in the remaining phases follow a similar pattern along the reactor axis. Alkanes and alkenes concentrations increase monotonically except the ethylene concentration which sharply increases in the first few meters but decreases next along the reactor. Alkanes are unreactive molecules, whereas ethylene is a more reactive molecule when compared with the remaining alkenes. Ethylene readsorbs on the catalyst and undergoes secondary reactions such as hydrogenation or chain growth.[46] The adequate description of the individual reactivities is possible thanks to the SEMK model applied.[16] The reactor model developed here can be used as a tool to monitor the species inside the reactor and optimize the production of individual molecules by modifying operating and/or design parameters.

The product distribution up to carbon number 9 at the reactor outlet is shown in Figure 4 for the different phases, that is, large bubbles, small bubbles, and slurry phase. The highest concentration of all the species up to carbon number 9 is present in the large bubbles, especially for the lighter products. The concentration of alkanes and alkenes decreases with the carbon number as it is typically observed in Fischer-Tropsch synthesis, which follows the so-called Anderson-Schulz-Flory product distribution. The concentration of ethylene is lower than that of propylene, as noticed also in Figure 3 and as it is observed experimentally.[47] The

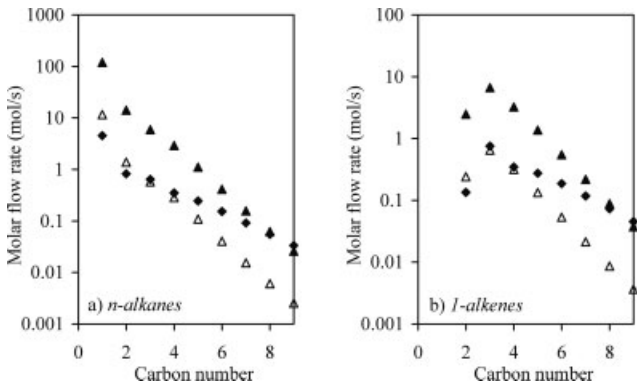

Figure 4. Molar flow rates at the reactor outlet for (a) *n*-alkanes and (b) 1-alkenes up to carbon number 9 in the large bubbles (▲), small bubbles (△) and slurry (◆) phase calculated with Eqs. 1–6 and Table 1 at the inlet and design conditions given in Table 4 with T^0 = 553 K, $\bar{\varepsilon}_{cat}$ = 0.25, F^0_{syngas} = 5 m^3/s, and $H_2/CO|^0$ = 2.

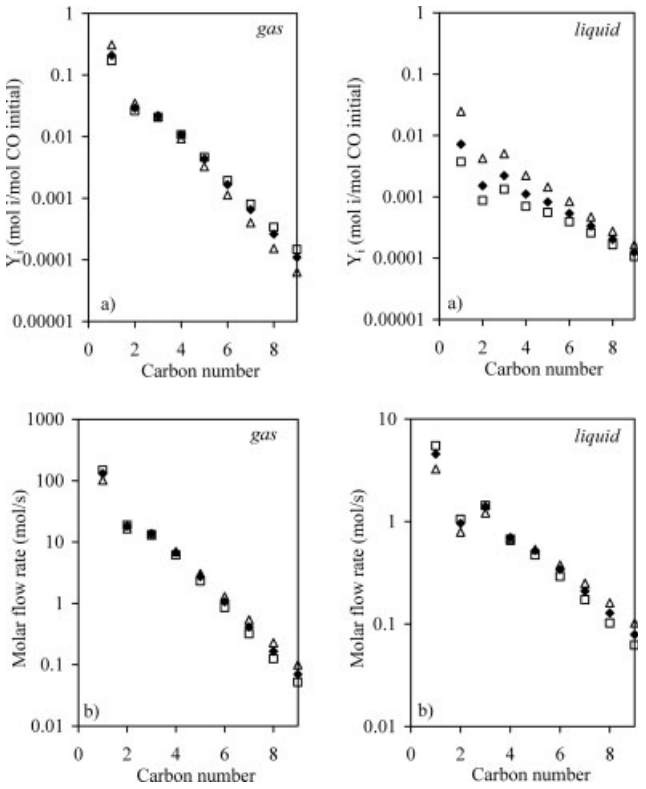

Figure 5. (a) Molar yields and (b) molar flow rates at the reactor outlet for hydrocarbons up to 9 carbon atoms in the gas and liquid phase at (a) a syngas feed flow rate, F^0_{syngas}, equal to 2 m^3/s (△), 5 m^3/s (◆), 8 m^3/s (□) at $\bar{\varepsilon}_{cat} = 0.25$, and at (b) an average catalyst hold-up, $\bar{\varepsilon}_{cat}$, equal to 0.15 (△), 0.25 (◆), 0.35 (□) at $F^0_{syngas} = 5\ m^3/s$, calculated with Eqs. 1–6 and Table 1 and at the inlet and design conditions given in Table 4 with $T^0 = 553$ K and $H_2/CO|^0 = 2$.

concentration of the species in the slurry phase decreases more moderately than in the gas phase because the vapor pressure of the heavier molecules decreases with the carbon number. Although for the C_2 fraction only the 5% mol/mol is present in the slurry phase, for the products beyond carbon number 10 the 62% mol/mol is in the slurry phase. The C_{10+} fraction constitutes 1.6% mol/mol of all the hydrocarbons in the slurry phase due to the catalyst used.

The effect of operating conditions such as average catalyst hold-up, syngas feed flow rate, temperature, and carbon monoxide to hydrogen inlet ratio are studied in Figures 5–7.

In Figure 5, the effect of the average catalyst hold-up and syngas feed flow rate on the gas and liquid product distributions is shown. The results of the gas phase displayed in Figures 5–7 include both the small and the large bubbles. In Figure 5, molar yields and molar flow rates of the hydrocarbons are given per carbon number in the gas and liquid phase at the reactor outlet. Again higher concentrations of the lighter molecules are observed in the gas phase. When decreasing the syngas feed flow rate, higher molar yields of lighter products are observed, more pronouncedly in the liquid phase, as well as a higher CO conversion, that is, 0.78 mol/mol of CO is converted at 2 m^3/s and 0.63 mol/mol of CO is converted at 8 m^3/s of fed syngas. When increasing the average catalyst hold-up, higher molar flow rates of the lighter products are observed, as well as a higher CO conversion, that is, 0.54 mol/mol of CO is converted at 0.15 m^3/m^3 and 0.74 mol/mol of CO is converted at 0.35 m^3/m^3 of average catalyst hold-up, respectively.

In Figure 6, the effect of the inlet temperature on the axial dimensionless superficial gas velocity and temperature, and on the molar yields of the hydrocarbons in the gas and the liquid phase, is shown. Higher temperatures cause higher conversions and as a result, lower superficial gas velocities, a higher axial temperature gradient inside the reactor and a higher outlet temperature. Also, the molar yield of the lighter hydrocarbons increases at higher inlet temperatures, for example, the calculated methane yield is 6.76×10^{-2} mol/mol at 523 K and 0.40 mol/mol at 583 K. Shorter hydrocarbons are preferentially formed according to the SEMK model at higher temperatures in line with

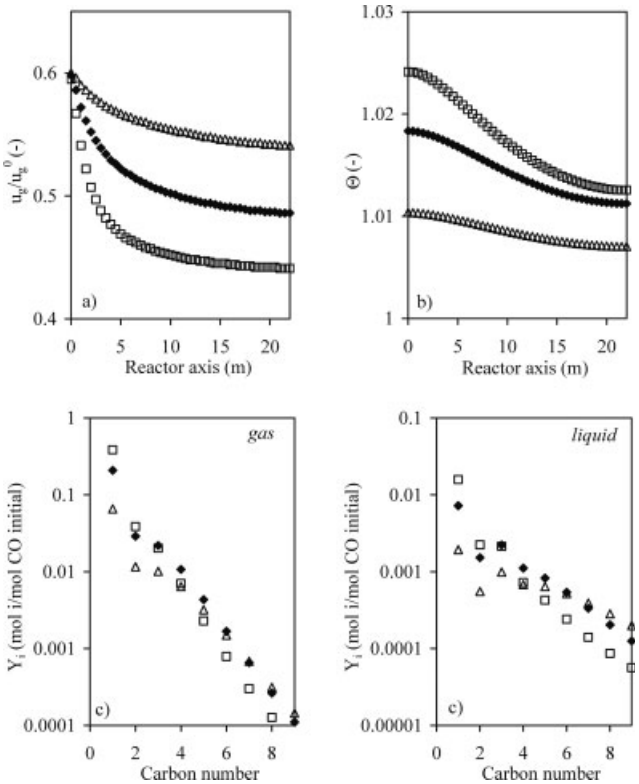

Figure 6. (a) Dimensionless superficial gas velocity, (b) dimensionless temperature profile, and (c) molar yields at the reactor outlet for hydrocarbons up to 9 carbon atoms in the gas and liquid phase, along the reactor axis at inlet temperature, T^0, equal to 523 K (△), 553 K (◆), and 583 K (□) calculated with Eqs. 1–6 and Table 1 at the inlet and design conditions given in Table 4 where $\bar{\varepsilon}_{cat} = 0.25$, $F^0_{syngas} = 5\ m^3/s$, and $H_2/CO|^0 = 2$.

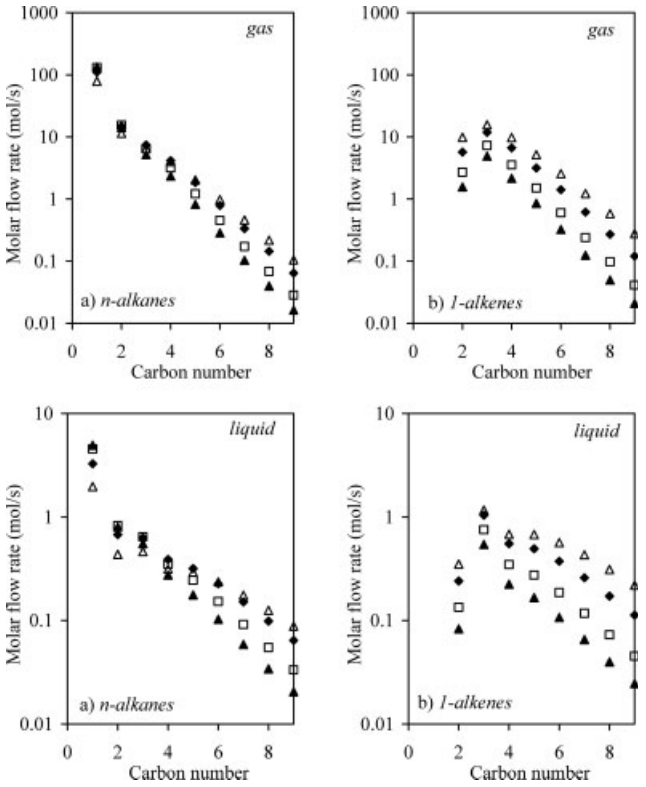

Figure 7. Molar flow rates at the reactor outlet for (a) *n*-alkanes and (b) 1-alkenes up to 9 carbon atoms in the gas and liquid phase at hydrogen to carbon monoxide inlet ratio, $H_2/CO|^\circ$, equal to 0.5 (△), 1.0 (◆), 2.0 (□), and 3.0 (▲) calculated with Eqs. 1–6 and Table 1 at the inlet and design conditions given in Table 4 with $T^0 = 553$ K, $\bar{\varepsilon}_{cat} = 0.25$, and $F^0_{syngas} = 5\ m^3/s$.

experimental observations.[46] The activation energies in the rate coefficients of the SEMK model have been estimated by model regression to experimental data, as discussed in a previous section. Activation energy values obtained for the chain termination leading to alkanes and alkenes (Eqs. 22 and 23 in Table 3) are higher than for the chain growth (Eq. 21 in Table 3),[16] hence, at higher temperatures the termination rate becomes relatively higher. This is most evident for the products with the lower carbon numbers, that is, the products formed in the first instance according to the reaction network based on the Anderson-Schulz-Flory distribution given in Table 3. The surface intermediates leading to the lower hydrocarbons have a higher concentration on the catalyst surface because they are formed first, that is, higher hydrocarbons are formed through a polymerization type or reaction (chain growth, Eq. 21 in Table 3). Hence, the net rate of termination to lighter hydrocarbons will be relatively higher than that of the higher hydrocarbons. This effect is observed in the gas as well as in the liquid phase.

The effect of the hydrogen to carbon monoxide inlet ratio on the product distribution is shown in Figure 7. In this case, molar outlet flow rates for *n*-alkanes and 1-alkenes are displayed in both gas and liquid phase. Molar flow rates from carbon number three onwards for 1-alkenes are higher than for *n*-alkanes. This becomes more evident at lower H_2/CO inlet molar ratios. In Figure 7, opposite effects are observed for *n*-alkanes at low and high carbon number in both phases. At higher hydrogen to carbon monoxide inlet ratios, the outlet flow rate of the lighter alkanes, particularly methane, increases, whereas the outlet flow rate of the heavier alkanes decreases. A decrease in the outlet flow rates is also observed for all 1-alkenes. This effect can be easily explained by assessing the concentrations of the catalyst surface intermediates. In Figure 8, the surface coverage of all the intermediate species involved in the Fischer-Tropsch synthesis reaction network given in Table 3 are displayed at different hydrogen to carbon monoxide inlet ratios. At higher hydrogen to carbon monoxide ratios, the concentration of hydrogen adatoms, θ_{M-H}, increases substantially. This will hinder chain growth by reaction of two hydrocarbon species (Eq. 21 in Table 3), and will favor the reductive elimination (Eq. 22 in Table 3) of the small hydrocarbon moieties present on the surface with hydrogen to give methane and to a minor extent, ethane and propane. However, at low hydrogen to carbon monoxide ratios, the fastest reaction will be the chain growth due to the deficiency in hydrogen adatoms to undergo reductive elimination to yield alkanes. β-hydride elimination to give alkenes (Eq. 23 in Table 3) will be favored likewise at low hydrogen to carbon monoxide inlet ratios. As it is observed in Figure 8, the concentration of alkyls, $\theta_{M-C_nH_{2n+1}}$, and alkenes, $\theta_{M-C_nH_{2n}}$, is maximum at low hydrogen to carbon monoxide ratios.

In summary, operating conditions and design parameters can be investigated with the simulation tool developed in this work, to optimize selectivities and/or increase capacities of individual products.

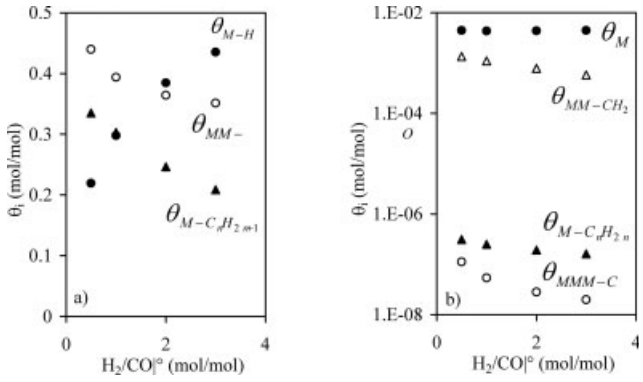

Figure 8. Surface coverage for (a) (●) hydride, (○) oxide, (▲) alkyls, and (b) (●) free surface atoms of the active phase, (△) methylene, (▲) alkenes, and (○) carbide species (*vide* reaction network in Table 3), at different hydrogen to carbon monoxide inlet ratios, $H_2/CO|^\circ$, calculated with Eqs. 1–6 and Table 1 at the inlet and design conditions given in Table 4 with $T^0 = 553$ K, $\bar{\varepsilon}_{cat} = 0.25$, and $F^0_{syngas} = 5\ m^3/s$.

Conclusions

An industrial slurry bubble column reactor for Fischer-Tropsch synthesis can be modeled using a fundamental Single-Event Microkinetic (SEMK) model. The use of a two-bubble size heterogeneous model with effective axial diffusion allows an adequate simulation of the slurry bubble column reactor for an iron-based catalyst. The individual rates of formation of every species, including the water-gas shift, can be assessed through the model equations. The simulation tool has been used for a reaction network up to 10 carbon atoms but it can support reaction networks with higher carbon numbers once the simulation time is optimized.

The effect of the reactor design parameters and operating conditions such as the average catalyst hold-up, syngas feed flow rate, inlet temperature, or hydrogen to carbon monoxide inlet ratio has been investigated.

At the bottom of the reactor, the conversion and product distribution is mass transfer controlled between large bubbles and the slurry phase. Few meters further, large bubbles are in equilibrium with the liquid phase and the process is kinetically controlled. Alkanes and alkenes concentrations increase monotonically along the reactor except for ethylene, which sharply increases in the first few meters and next decreases due to its readsorption and further reaction on the catalyst surface. At the reactor outlet, the species are mostly found in the large bubbles, particularly the lighter products, while the heavier products, beyond carbon number 9, will be mostly located in the liquid phase.

Higher CO conversions and higher molar yields of lighter hydrocarbons are obtained when increasing the catalyst loading or decreasing the syngas feed flow rate, which translates into a higher axial temperature and superficial gas velocity gradient inside the reactor. At higher inlet temperatures and higher hydrogen to carbon monoxide inlet ratios, shorter hydrocarbons are preferentially formed. The temperature effect is the consequence of the higher SEMK activation energies for the chain termination to alkanes and alkenes when compared with the chain growth activation energy.

The effect of the hydrogen to carbon monoxide inlet ratio can be explained also in terms of surface coverage. At higher hydrogen to carbon monoxide ratios, a higher coverage of hydrogen adatoms is generated and this hinders chain growth reaction while it favors the reductive elimination of the small hydrocarbon surface species to light alkanes.

Acknowledgments

G.L.-B. thanks IFP for financial support. This research has been partly carried out in the framework of the Interuniversity Attraction Poles Programme funded by the Belgian Science Policy, and partly supported by the European research project "TOPCOMBI" (contract NMP2-CT2005-515792).

Notation

Roman symbols

$a_{LB/SB}$ = gas-liquid interfacial surface area for the large bubbles or small bubbles referred to the total liquid volume (m^2/m^3)

a_w = volumetric heat exchange surface area for the cooling tubes (m^2/m^3)

Ar = Archimedes number $\left((\rho_{cat}-\rho_L)\rho_L g d_{cat}^3/\eta_L^2\right)$ (−)

Bo = Bodenstein number $\left(Pe_{cat}\left[\frac{u_{CT}}{u_{g,int}}-\frac{u_{SL}}{u_{g,int}(i-\varepsilon_g)}\right]\right)$ (−)

Be = dimensionless heat of reaction $\left(\left(-\Delta H_{R_i}^0\right)C_g^0/\rho_{SL}C_{p,SL}He_jT_w\right)$ (−)

C = concentration (mol/kg_{cat} or mol/m^3_R)

c_p = specific heat (J/kg K)

$D_{L,j}$ = molecular diffusivity of solute j in the liquid (m^2/s)

d = diameter (m)

d_R = reactor diameter (m)

E = axial effective diffusion coefficient (m^2/s)

F = molar flow rate (mol/s)

Fr = Froude number $\left(u_g/(gd_R)^{0.5}\right)$ (−)

ΔH_R^0 = standard reaction enthalpy (kJ/mol)

Δh = finite spatial difference (m)

H = column height (m)

He = Henry coefficient (bar)

He^∞ = Henry coefficient at infinite dilution (bar)

k = kinetic coefficient of an elementary step (bar^{-1} s^{-1} or s^{-1})

k_g = gas mass transfer coefficient at the gas/liquid interface (m/s)

k_L = liquid mass transfer coefficient at the gas/liquid interface (m/s)

M_w = molecular mass (kg/mol)

n = number or carbon number

nint = number of intermediate species

nmalkyl = number of metal alkyl species

nr = number of independent reactions

p = pressure (bar)

Pe_{cat} = Peclet number for catalyst particles $\left(u_g^0 H/E_{cat}\right)$ (−)

Pe_{LB}^g = Peclet number for large bubbles $\left(u_g^0 H/E_{G,LB}\right)$ (−)

Pe_{SB}^g = Peclet number for small bubbles $\left(u_g^0 H/E_{g,SB}\right)$ (−)

Pe_H = Peclet number for heat transfer $\left(\rho_{SL}C_{p,SL}u_g^0 H/\lambda_{ax}\right)$ (−)

Pe_L = Peclet number for liquid phase $\left(u_g^0 H/E_L\right)$ (−)

R = net production rate (mol/kg_{cat} s)

$\hat{r}$ = dimensionless reaction rate (−)

Re = Reynolds number for a catalyst particle $(u_{CT}d_{cat}/\nu_L)$ (−)

St_H = Stanton number for heat transfer $\left(\alpha_{eff}a_w H/\rho_{SL}c_{p,SL}u_g^0\right)$ (−)

$St_{LB/SB,j}^g$ = Stanton number, gas side for species j in the large bubbles/small bubbles $\left(k_{LB/SB,j}^L a_{LB/SB}H/u_g^0 He_j^0\right)$ (−)

$St_{LB/SB,j}^L$ = Stanton number, liquid side for species j in the large bubbles/small bubbles $\left(k_{LB/SB,j}^L a_{LB/SB}H/u_g^0\right)$ (−)

T = temperature (K)

T_w = temperature of the cooling tubes (K)

u = superficial velocity (m/s)

u_{CT} = settling velocity of the catalyst (m/s)

u_{TS} = terminal settling velocity (m/s)

v = molar volume (cm^3/g mol)

$\bar{v}_i^\infty$ = partial molar volume at infinite dilution (cm^3/g mol)

V_{SB} = rise velocity of small bubbles (m/s)

W_{cat} = mass fraction of the catalyst (kg/kg)

x_j = dimensionless concentration of species j in the liquid $\left(C_{L,j}He_j/C_g^0\right)$ (mol/mol)

X = conversion (mol/mol)

$y_{LB,j}$ = dimensionless concentration of species j in the large bubbles $\left(C_{LB,j}/C_g^0\right)$ (mol/mol)

$y_{SB,j}$ = dimensionless concentration of species j in the small bubbles $\left(C_{SB,j}/C_g^0\right)$ (mol/mol)

Y = molar yield (mol/mol CO initial)

z = number of nearest neighbor atoms on the surface
z_c = axial position in the column (m)

Constants

G = gravitational acceleration (9.8 m/s^2)
R = universal gas constant (8.3144 J/mol K)

Greek letters

α_c = contraction factor (−)
α_{eff} = effective axial heat dispersion (W/m^{2}K)
γ = activity coefficient (−)
ε = hold-up ($m^3_{phase}/m^3_{reactor}$)
ε_{cat} = catalyst hold-up in the slurry (m^3_{cat}/m^3_{SL})
$\bar{\varepsilon}_{cat}$ = average catalyst hold-up in the reactor (m^3_{cat}/m^3_{SL})
ε^*_{cat} = catalyst hold-up in the slurry when ρ_{cat} is 100 kg/m^3 (m^3_{cat}/m^3_{SL})
η = viscosity (Pa s)
θ_k = degree of coverage of species k ($mol_k/mol_{active\ sites}$)
Θ = dimensionless temperature (T/T_w) (−)
λ = heat conductivity (W/mK)
ν = kinematic viscosity (m^2/s)
ξ = dimensionless axial position in the reactor (z_c/H) (−)
ρ = density (kg/m^3)
σ = gas–liquid surface tension (N/m)
σ_r = global symmetry number of reactant(s)
$\sigma_{\neq}$ = global symmetry number of transition state complex
τ = dimensionless time $\left(tu_g^0/H\right)$ (−)
υ = Stoichiometric coefficient
Φ = Poynting factor (−)

Subscripts

ax = axial
cat = catalyst
chem = chemisorption
des = desorption
g = gas
gl = global
L = liquid phase
LB = large bubbles
M = metal atom
M—H = metal hydride
MM—CH_2 = metal methylene
M—C_nH_{2n} = metal alkene
M—C_nH_{2n+1} = metal alkyl
MMM—C = metal carbide
M—O = metal oxide
R = reactor
re = reductive elimination
ref = reference
SB = small bubbles
SL = slurry
tot = total
trans = transition from homogeneous to heterogeneous flow regime

Superscripts

$\sim$ = single-event
$\neq$ = transition state
0 = initial, inlet or standard (0.1 MPa)

Literature Cited

1. Dry ME. Present and future applications of the Fischer-Tropsch process. *Appl Catal A-Gen*. 2004;276:1–3.
2. Dry ME, Steynberg AP. Commercial Fischer-Tropsch process applications. *Stud Surf Sci Catal*. 2004;152:406–481.
3. Steynberg AP, Dry ME, Davis BH, Breman BB. Fischer-Tropsch reactors. *Stud Surf Sci Catal*. 2004;152:64–195.
4. de Swart JWA, Krishna R, Sie ST. Selection, design and scale up of the Fischer-Tropsch reactor. *Nat Gas Conversion IV*. 1997;107:213–218.
5. de Swart JWA, Krishna R. Simulation of the transient and steady state behaviour of a bubble column slurry reactor for Fischer-Tropsch synthesis. *Chem Eng Process*. 2002;41:35–47.
6. Krishna R, Maretto C. Scale up of a bubble column slurry reactor for Fischer-Tropsch synthesis. *Nat Gas Conversion V*. 1998;119:197–202.
7. Krishna R, Sie ST. Design and scale-up of the Fischer-Tropsch bubble column slurry reactor. *Fuel Process Technol*. 2000;64:73–105.
8. Maretto C, Krishna R. Modelling of a bubble column slurry reactor for Fischer-Tropsch synthesis. *Catal Today*. 1999;52:279–289.
9. Rados N, Al-Dahhan MH, Dudukovic MP. Modeling of the Fischer-Tropsch synthesis in slurry bubble column reactors. *Catal Today*. 2003;79:211–218.
10. Rados N, Al-Dahhan MH, Dudukovic MP. Dynamic modeling of slurry bubble column reactors. *Ind Eng Chem Res*. 2005;44:6086–6094.
11. Ahon VR, Costa EF, Monteagudo JEP, Fontes CE, Biscaia EC, Lage PLC. A comprehensive mathematical model for the Fischer-Tropsch synthesis in well-mixed slurry reactors. *Chem Eng Sci*. 2005;60:677–694.
12. Mills PL, Turner JR, Ramachandran PA, Dudukovic MP. The Fischer-Tropsch synthesis in slurry bubble column reactors: analysis of reactor performance using the axial dispersion model. In: Nigam KDP, Schumpe A, editors. *Three-Phase Sparged Reactors*. Amsterdam: Gordon and Breach, 1996:339–386.
13. van der Laan GP, Beenackers AACM, Krishna R. Multicomponent reaction engineering model for Fe-catalyzed Fischer-Tropsch synthesis in commercial scale slurry bubble column reactors. *Chem Eng Sci*. 1999;54:5013–5019.
14. Iliuta I, Larachi F, Anfray J, Dromard N, Schweich D. Multicomponent multicompartment model for Fischer-Tropsch SCBR. *AIChE J*. 2007;53:2062–2083.
15. Lozano-Blanco G, Thybaut JW, Surla K, Galtier P, Marin GB. Fischer-Tropsch synthesis: development of a microkinetic model for metal catalysis. *Oil Gas Sci Technol-Rev IFP*. 2006;61:489–496.
16. Lozano-Blanco G, Thybaut JW, Surla K, Galtier P, Marin GB. Single-event microkinetic model for Fischer-Tropsch synthesis on iron-based catalysts. *Ind Eng Chem Res*. 2008;47:5879–5891.
17. Kato Y, Nishiwaki T, Fukuda T, Tanaka S. The behaviour of suspended solid particles and liquid in bubble columns. *J Chem Eng Jpn*. 1972;5:112–118.
18. Danckwerts PV. Significance of liquid-film coefficients in gas absorption. *Ind Eng Chem*. 1951;43:1460–1467.
19. Deckwer WD, Louisi Y, Zaidi A, Ralek M. Hydrodynamic properties of the Fischer-Tropsch slurry process. *Ind Eng Chem Process Des Dev*. 1980;19:699–708.
20. Deckwer WD, Serpemen Y, Ralek M, Schmidt B. Modeling the Fischer-Tropsch synthesis in the slurry phase. *Ind Eng Chem Process Des Dev*. 1982;21:231–241.
21. Lox ES, Marin GB, Degrave E, Bussiere P. Characterization of a promoted precipitated iron catalyst for Fischer-Tropsch synthesis. *Appl Catal*. 1988;40:197–218.
22. Post MFM, Vanthoog AC, Minderhoud JK, Sie ST. Diffusion limitations in Fischer-Tropsch catalysts. *AIChE J*. 1989;35:1107–1114.
23. Benson SW. *Thermochemical Kinetics: Methods for the Estimation of Thermochemical Data and Rate Parameters*. New York: John Wiley, 1968.
24. Lide DR. *CRC Handbook of Chemistry and Physics: A Ready-Reference Book of Chemical and Physical Data, 84th ed.* Boca Raton, FL, London: CRC, 2003.
25. Wilke CR, Chang P. Correlation of diffusion coefficients in dilute solutions. *AIChE J*. 1955;2:264–270.
26. Poling BE, Prausnitz JM, O'Connell JP, Reid RC. *The Properties of Gases and Liquids, 5th ed*. New York; London: McGraw-Hill, 2001.
27. Smith JM, Van Ness HC, Abbott M. *Introduction to Chemical Engineering Thermodynamics, 5th ed*. New York; London: McGraw-Hill, 1996.
28. Marano JJ, Holder GD. Characterization of Fischer-Tropsch liquids for vapor-liquid equilibria calculations. *Fluid Phase Equilib*. 1997;138:1–21.
29. Levenspiel O. *Chemical Reaction Engineering*. New York, London: Wiley, 1972.
30. Krishna R, Ellenberger J. Gas holdup in bubble column reactors operating in the churn-turbulent flow regime. *AIChE J*. 1996;42: 2627–2634.
31. Wilkinson PM, Spek AP, Vandierendonck LL. Design parameters estimation for scale-up of high-pressure bubble-columns. *AIChE J*. 1992;38:544–554.

32. Letzel MH. Effect of gas density on large-bubble holdup in bubble column reactors. *AIChE J*. 1998;44:2333–2336.
33. Calderbank PH, Moo-Young MB. The continuous phase heat and mass-transfer properties of dispersions. *Chem Eng Sci*. 1961;16:39–54.
34. Wilkinson PM, Haringa H, Vandierendonck LL. Mass-transfer and bubble-size in a bubble-column under pressure. *Chem Eng Sci*. 1994;49:1417–1427.
35. Vermeer DJ, Krishna R. Hydrodynamics and mass-transfer in bubble-columns operating in the churn-turbulent regime. *Ind Eng Chem Process Des Dev*. 1981;20:475–482.
36. Vynckier E, Froment GF. Modeling of the kinetics of complex processes based upon elementary steps. In: Astarita G, Sandler SI, editors. *Kinetic and Thermodynamic Lumping of Multicomponent Mixtures: Proceedings of an ACS Symposium on Kinetic and Thermodynamic Lumping of Multicomponent Mixtures (Atlanta)*. Amsterdam: Elsevier, 1991.
37. Brady RC, Pettit R. On the mechanism of the Fischer-Tropsch reaction—the chain propagation step. *J Am Chem Soc*. 1981;103:1287–1289.
38. Rethwisch DG, Dumesic JA. The effect of metal-oxygen bond strength on properties of oxides. 2. Water-gas shift over bulk oxides. *Appl Catal*. 1986;21:97–109.
39. Lox ES, Froment GF. Kinetics of the Fischer-Tropsch reaction on a precipitated promoted iron catalyst. 1. Experimental procedure and results. *Ind Eng Chem Res*. 1993;32:61–70.
40. Froment GF, Bischoff KB. *Chemical Reactor Analysis and Design*, 2nd ed. New York: Wiley, 1990.
41. Boudart M, Djéga-Mariadassou G. *Kinetics of Heterogeneous Catalytic Reactions*. Princeton, N.J.: Princeton University Press, 1984.
42. Schiesser WE. *The Numerical Method of Lines: Integration of Partial Differential Equations*. San Diego: Academic Press, 1991.
43. http://netlib.org.
44. Powell MJD. *A Hybrid Method for Nonlinear Equations.* London: Gordon and Breach, 1970.
45. Behkish A, Lemoine R, Sehabiague L, Oukaci R, Morsi BI. Gas holdup and bubble size behavior in a large-scale slurry bubble column reactor operating with an organic liquid under elevated pressures and temperatures. *Chem Eng J*. 2007;128:69–84.
46. Kuipers EW, Vinkenburg IH, Oosterbeek H. Chain-length dependence of alpha-olefin readsorption in Fischer-Tropsch synthesis. *J Catal*. 1995;152:137–146.
47. Anderson RB. *The Fischer-Tropsch Synthesis*. New York: Academic Press, 1984.

Manuscript received Jun. 19, 2008, and revision received Nov. 24, 2008.